

Dynamics, CO depletion, and deuterium fractionation of the dense condensations within the fragmented prestellar core Orion B9–SMM 6[★]

O. Miettinen¹ and S. S. R. Offner^{2**}

¹ Department of Physics, University of Helsinki, P.O. Box 64, FI-00014 Helsinki, Finland
e-mail: oskari.miettinen@helsinki.fi

² Department of Astronomy, Yale University, New Haven, CT 06511, USA
e-mail: stella.offner@yale.edu

Received ; accepted

ABSTRACT

Context. Low-mass prestellar cores are rarely found to be fragmented into smaller condensations but studying such substructure where present is essential for understanding the origin of multiple stellar systems.

Aims. We attempt to better understand the kinematics and dynamics of the subfragments inside the prestellar core SMM 6 in Orion B9. Another object of the present study is to constrain the evolutionary stage of the condensations by investigating the levels of CO depletion and deuterium fractionation.

Methods. We used the APEX telescope to observe the molecular lines C¹⁷O(2 – 1), N₂H⁺(3 – 2), and N₂D⁺(3 – 2) towards the condensations. We use the line data in conjunction with our previous SABOCA 350- μ m dust continuum map of the source.

Results. The condensations are characterised by subsonic internal non-thermal motions ($\sigma_{\text{NT}} \simeq 0.5c_s$), and most of them appear to be gravitationally bound. The dispersion of the N₂H⁺ velocity centroids among the condensations is very low (0.02 km s⁻¹). The CO depletion factors we derive, $f_{\text{D}} = 0.8 \pm 0.4 - 3.6 \pm 1.5$, do not suggest any significant CO freeze-out but this may be due to the canonical CO abundance we adopt. The fractional abundances of N₂H⁺ and N₂D⁺ with respect to H₂ are found to be $\sim 0.9 - 2.3 \times 10^{-9}$ and $\sim 4.9 - 9.9 \times 10^{-10}$, respectively. The deuterium fractionation of N₂H⁺ lies in the range $0.30 \pm 0.07 - 0.43 \pm 0.09$.

Conclusions. The detected substructure inside SMM 6 is likely the result of cylindrical Jeans-type gravitational fragmentation. We estimate the timescale for this fragmentation to be $\sim 1.8 \times 10^5$ yr. The condensations are unlikely to be able to interact with one another and coalesce before local gravitational collapse ensues. Moreover, significant mass growth of the condensations via competitive-like accretion from the parent core seems unfeasible. The high level of molecular deuteration in the condensations suggests that gas-phase CO should be strongly depleted. It also points towards an advanced stage of chemical evolution. The subfragments of SMM 6 might therefore be near the onset of gravitational collapse, but whether they can form protostellar or substellar objects (brown dwarfs) depends on the local star formation efficiency and remains to be clarified.

Key words. Astrochemistry – Stars: formation – ISM: individual objects: Orion B9–SMM 6 – ISM: kinematics and dynamics – ISM: molecules

1. Introduction

Fragmentation of interstellar molecular clouds appears to occur in a hierarchical fashion. Recent *Herschel* observations have clearly demonstrated that on the scales of several parsecs to ~ 10 pc the cloud structures are highly filamentary in shape (e.g., André et al. 2010; Arzoumanian et al. 2011; Hill et al. 2011; Palmeirim et al. 2013). The origin of large-scale filaments is still unclear, but they often (if not always) show substructures along their long axes. Substructures on scales of $\sim 0.5 - 1$ pc are typically called *clumps*, which may contain significant gas substructure and would likely form a cluster of stars. Gas fragments ≤ 0.1 pc, which are expected to form a single star or bound multiple system, are called *cores*.

The dense cores formed in the course of hierarchical fragmentation represent the size scale on which protostellar collapse and the formation of low-mass ($\sim 0.1 - 2 M_{\odot}$) stars take place. Initially starless cores that are bound by their self-gravity are called *prestellar cores* (Ward-Thompson et al. 1994). These are ideal laboratories to study the genuine initial physical and chemical conditions of star formation. Because many stars are found in binary or higher-order multiple systems (e.g., Raghavan et al. 2010; Kraus & Hillenbrand 2012; Duchêne & Kraus 2013), core fragmentation into still smaller subunits is expected to occur at some point in their evolution, possibly during the prestellar phase. In the present work, we will use the term *condensation* for such subfragments with sizes of ~ 0.01 pc (e.g., André et al. 2007, hereafter ABMP07). Since condensations are fairly low-mass and are usually found within a gravitationally bound core, they likely represent the precursors of individual stars that will eventually comprise a multiple star system.

Core fragmentation is of prime importance when studying the origin of core mass function and its connection to the stellar initial mass function (IMF). From a theoretical point of view, the

* This publication is based on data acquired with the Atacama Pathfinder Experiment (APEX) under programmes 079.F-9313(A), 084.F-9312(A), and 090.F-9313(A). APEX is a collaboration between the Max-Planck-Institut für Radioastronomie, the European Southern Observatory, and the Onsala Space Observatory.

** Hubble Postdoctoral Fellow.

formation of multiple stellar systems is far from well-understood (e.g., Tohline 2002; Goodwin et al. 2007). For example, the initial phase and characteristic timescale of the fragmentation process remain to be established. Observationally, it is unclear how common the fragmentation of low-mass cores actually is, particularly in the case of starless/prestellar cores.

Some of the earliest instances of core substructure were discovered by Lemme et al. (1995). They mapped the starless core L1498 in the C-bearing molecules $C^{18}O$ and CS using the IRAM 30-m telescope with $12'' - 25''$ resolution. The core was resolved into many small-scale condensations with diameters and masses of about 0.02 pc and $0.01 M_{\odot}$, respectively. The subfragments were found to be gravitationally unbound, and the authors suggested that they are just transient structures (see also Kuiper et al. 1996). Langer et al. (1995) used high-resolution ($6'' - 9''$) interferometric observations to map the TMC-1 core D. Similarly to L1498, the core was found to be composed of several condensations with sizes and masses of $0.007 - 0.021$ pc and $\sim 0.01 M_{\odot}$, respectively. These sources were also found to be gravitationally unbound and unable to form even protobrown dwarfs unless the condensations were to merge and form more massive structures. Langer et al. (1995) suggested that a pure Jeans-type gravitational instability could not be responsible for the core fragmentation. However, the substructure was identified from molecular-line maps (the C-bearing species CCS and CS). Therefore, it is possible that the subfragments represent small-scale chemical inhomogeneities of the parent core (cf. Takakuwa et al. 1998).

Kamazaki et al. (2001) detected the first subfragments inside prestellar cores in dust emission. They carried out high-resolution NMA observations of 2- and 3-mm dust continuum emission towards two prestellar cores in the ρ Oph A region, namely SM1 and SM1N. Both cores appeared to contain condensations of $600 - 1100$ AU in size with masses in the range $0.054 - 0.14 M_{\odot}$. Interestingly, as opposed to the above mentioned studies, the condensations found by Kamazaki et al. (2001) were determined to be gravitationally bound entities. We note that one of the condensations within SM1, with a mass of $0.14 M_{\odot}$, was suggested by the authors to be already in the early protostellar phase. Kamazaki et al. (2001) also concluded that the substructures were the result of gravitational fragmentation of the parent cores. Takakuwa et al. (2003) studied two prestellar cores in the TMC-1C region with high-resolution molecular-line observations, and found ~ 2500 AU -size condensations with masses of $\sim 0.02 M_{\odot}$ inside the cores. These substellar-mass fragments were found to be gravitationally unbound but with dissipation timescales long enough to allow the fragments to coalesce with one another and form more massive objects.

More recently, Kirk et al. (2009) studied the prestellar core L183 (L134N) with high-resolution ($13'' \times 10''$ or ~ 0.006 pc ~ 1200 AU) BIMA interferometric observations, and found it to be composed of three condensations of $\sim 0.005 - 0.01$ pc in radii. They concluded that the observed substructure was the result of the fragmentation of a rotating and collapsing prestellar core. On the other hand, Schnee et al. (2010) found that none of their 11 starless cores in Perseus break into smaller components at $5''$ resolution or on the $\sim 10^3$ AU scale (see also Miettinen & Offner 2013 for Ori B9–SMM 1). Chen & Arce (2010), using SMA observations at $5''.7 \times 2''.3$ resolution (~ 0.003 pc or ~ 620 AU), discovered three condensations inside the prestellar core R CrA SMM 1A. The projected separation between the $0.1 - 0.2 M_{\odot}$ mass condensations was found to be between 1000 and 2100 AU. The observed spacings are comparable to the local Jeans length, and the authors suggested that

the condensations were formed through the fragmentation of an elongated prestellar core during the isothermal phase of evolution (i.e., when the radiative cooling is able to compensate for the heating by compression). Nakamura et al. (2012) used the SMA with a few arcsec (a few hundred AU) resolution to observe the prestellar cores SM1 and B2-N5 in ρ Ophiuchus (cf. Kamazaki et al. 2001). These cores were resolved into three and four condensations, respectively, with masses of $\sim 0.01 - 0.1 M_{\odot}$ and sizes of a few hundred AU. The masses were determined to be high enough for the condensations to be gravitationally bound. Nakamura et al. (2012) proposed that the origin of the substructures could be explained by turbulent fragmentation (e.g., Fisher 2004; Offner et al. 2010).

The target source of the present study is the prestellar core SMM 6 in the Orion B9 star-forming region. It was originally discovered by Miettinen et al. (2009; hereafter, Paper I) from the LABOCA $870\text{-}\mu\text{m}$ mapping of Orion B9. The core was found to be elongated in shape and not harbouring any embedded infrared point source, and we suggested that it is likely to be prestellar due its high density. Based on the NH_3 observations with the Effelsberg 100-m telescope, Miettinen et al. (2010; henceforth, Paper II) derived the gas kinetic temperature of $T_{\text{kin}} = 11.0 \pm 0.4$ K towards a selected position in SMM 6. The one-dimensional non-thermal velocity dispersion was derived to be 0.1 km s^{-1} , which is subsonic by a factor of two. Employing the new temperature value with the assumption that T_{kin} equals the dust temperature (T_{dust}), the mass of SMM 6 was estimated to be $8.2 \pm 1.1 M_{\odot}$. The virial-parameter analysis of the source suggested that it is gravitationally bound and near virial equilibrium, supporting our earlier speculation that it is in the prestellar phase of evolution.¹ Miettinen et al. (2012; hereafter, Paper III) presented further molecular-line observations towards the NH_3 target position in SMM 6. The CO depletion factor was estimated to be 4.2 ± 1.3 , and the N_2D^+/N_2H^+ column density ratio was found to be $\sim 0.6 \pm 0.1$, indicating a high degree of deuterium fractionation. In Paper III, we also presented the results of our SABOCA $350\text{-}\mu\text{m}$ imaging of dense cores in Orion B9. SMM 6, determined to be a thermally supercritical cylindrical object, was resolved into three to four very low-mass (revised masses are $\sim 0.2 - 0.6 M_{\odot}$; see Appendix A) condensations projectively separated by ~ 0.06 pc or $\sim 1.2 \times 10^4$ AU (see Fig. 1)². The origin of this substructure can be explained in terms of thermal Jeans-type fragmentation. It seems likely that SMM 6 has undergone a similar fragmentation process as R CrA SMM 1A described above. In Table 1, we list the SABOCA $350\text{-}\mu\text{m}$ peak positions of the SMM 6's condensations along with their main physical properties.

Recent *Herschel* data show that SMM 6 belongs to a northeast-southwest oriented filamentary structure (see Fig. 2). Miettinen (2012b) found that there is a sharp velocity gradient in the parent filament (across its short axis), and suggested that it might represent a shock front resulting from the feedback from the nearby expanding H II region NGC 2024 (~ 4 pc southwest of Orion B9). The formation of dense cores in Orion B9, including SMM 6, might have been triggered by this feedback. As highlighted in Fig. 2, the ring-like cloud structure consisting partly of SMM 6 could be a manifestation of such a dynamic environment.

¹ The core mass is revised down by a factor of ~ 1.4 in the present paper. This does not affect its classification into a gravitational bound or prestellar core (Appendix A).

² We assumed that the distance to Orion B9 is $d = 450$ pc. This value is also adopted in the present paper.

In Paper III, we noticed that our LABOCA map employed in Papers I and II was misaligned, and therefore we had to adjust its pointing using the *Spitzer* and SABOCA source positions (see footnote 2 in Paper III and Miettinen & Offner 2013). The target positions of our previous molecular-line observations were chosen to be the peak positions of the LABOCA map before adjusting the pointing, and therefore they are slightly offset from the 870- μm maxima. In the case of SMM 6, our previous line observations probed the core edge (as shown by the green plus sign in Fig. 1). To better understand the physics and chemistry of SMM 6, particularly the properties of its substructure, we performed follow-up molecular-line observations towards the condensations. In the present paper, we examine the kinematics and dynamics of these subfragments and their chemical properties, namely CO depletion and molecular deuteration of N_2H^+ . The latter parameter has the potential to constrain the evolutionary stage of the condensations (e.g. Crapsi et al. 2005; Friesen et al. 2013). The present work is one of the first studies of the dynamics of subfragments within a prestellar core. The observations and data reduction are described in Sect. 2. Section 3 presents the observational results, while analysis and its results are presented in Sect. 4 and Appendix A. We discuss the results in Sect. 5 and in Sect. 6, we summarise the paper and draw our main conclusions.

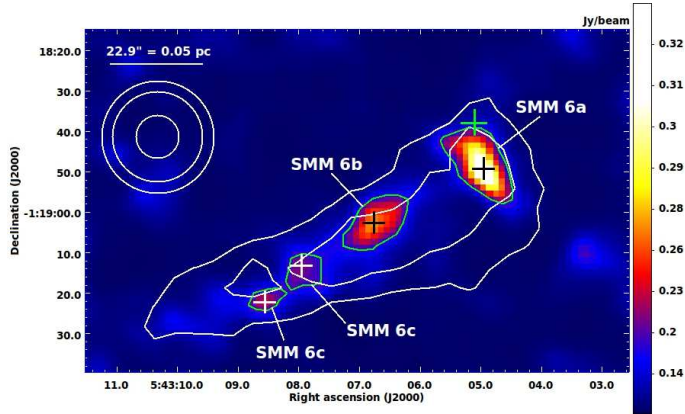


Fig. 1. SABOCA 350- μm image of the fragmented prestellar core SMM 6 in Orion B9. The image is displayed with power-law scaling, and the colour bar indicates the surface-brightness scale in Jy beam^{-1} . The overlaid green SABOCA contours are plotted at three times the noise level ($3\sigma = 180 \text{ mJy beam}^{-1}$). The white contours show the *Herschel*/SPIRE 250- μm dust continuum emission ($18''$ resolution); these contours are plotted at 3.0 and 3.5 Jy beam^{-1} . The green plus sign indicates the target position of our previous molecular-line observations, while the other plus signs mark the target positions of the present study (i.e., the 350- μm peaks). A scale bar indicating the 0.05 pc projected length is shown in the top left, with the assumption of a 450 pc line-of-sight distance. The three circles in the upper left corner show the effective FWHM of the SABOCA beam ($10''.6$), and the smallest ($22''.3$) and largest ($27''.8$) beamsizes of the present molecular-line observations.

2. Observations and data reduction

We used the APEX (Atacama Pathfinder EXperiment; Güsten et al. 2006) 12-m telescope in Chile to observe the spectral-line transitions $\text{C}^{17}\text{O}(2 - 1)$, $\text{N}_2\text{H}^+(3 - 2)$, and

$\text{N}_2\text{D}^+(3 - 2)$ towards the 350- μm peaks of the dense condensations within SMM 6. The N_2H^+ observations were carried out on 25 September 2012, while those of C^{17}O and N_2D^+ were performed on the 27th of the month. The strongest 350- μm condensation SMM 6a was observed again in C^{17}O on 28 September because the previous day’s weather was poor when the source was observed.

The observed transitions, their selected spectroscopic properties, and observational parameters are summarised in Table 2. The critical densities, $n_{\text{crit}} = A_{\text{ul}}/C_{\text{ul}}$, listed in Col. (4) of Table 2, were calculated at $T = 10 \text{ K}$ using the Einstein A -coefficients from the Leiden Atomic and Molecular Database (LAMDA; Schöier et al. 2005)³ (C^{17}O) and Pagani et al. (2009) (N_2H^+ and N_2D^+). The collisional-rate data (C_{ul}) were taken from LAMDA (C^{17}O) and the Caltech Submillimeter Wave Astrophysics website⁴ (N_2H^+ and N_2D^+). The latter are based on data from BASECOL (Dubernet et al. 2013)⁵.

As a frontend for the $\text{C}^{17}\text{O}(2 - 1)$ and $\text{N}_2\text{D}^+(3 - 2)$ observations, we used the APEX-1 receiver of the Swedish Heterodyne Facility Instrument (SHeFI; Belitsky et al. 2007; Vassilev et al. 2008a,b). APEX-1 operates in single-sideband (SSB) mode using sideband separation mixers, and it has a sideband rejection ratio $> 10 \text{ dB}$. For the $\text{N}_2\text{H}^+(3 - 2)$ observations the frontend used was APEX-2, which has similar characteristics as APEX-1. The backend for all observations was the RPG eXtended bandwidth Fast Fourier Transform Spectrometer (XFFTS; cf. Klein et al. 2012) with an instantaneous bandwidth of 2.5 GHz and 32 768 spectral channels.

The observations were performed in the wobbler-switching mode with a $100''$ azimuthal throw (symmetric offsets) and a chopping rate of 0.5 Hz. The telescope focus and pointing were optimised and checked at regular intervals on the planet Jupiter, and the variable stars W Orionis, RAFGL865 (V1259 Ori), α Ceti (Mira A), and R Leporis (Hind’s Crimson Star). The pointing was found to be accurate to $\sim 3''$. Calibration was made by means of the chopper-wheel technique and the output intensity scale given by the system is T_{A}^* , i.e., the antenna temperature corrected for the atmospheric attenuation. The observed intensities were converted to the main-beam brightness temperature scale by $T_{\text{MB}} = T_{\text{A}}^*/\eta_{\text{MB}}$, where η_{MB} is the main-beam efficiency. The absolute calibration uncertainty is estimated to be about 10%.

The spectra were reduced using the CLASS90 programme of the GILDAS software package⁶. The individual spectra were averaged and the resulting spectra were Hanning-smoothed to improve the signal-to-noise ratio. Linear (first-order) baselines were determined from velocity ranges without line-emission features, and then subtracted from the spectra. The resulting 1σ rms noise levels at the smoothed resolutions are listed in the last column of Table 2.

The $J = 2 - 1$ transition of C^{17}O contains nine hyperfine (hf) components that are spread over $\sim 2.4 \text{ km s}^{-1}$. We fitted this hf structure using “method hfs” of CLASS90 to derive the LSR velocity (v_{LSR}) of the emission, and FWHM linewidth (Δv). The hf line fitting can also be used to derive the line optical thickness by comparing the relative intensities of the hf components. However, in all spectra the hf components are mostly blended

³ <http://www.strw.leidenuniv.nl/~moldata/>

⁴ http://www.submm.caltech.edu/~tab/molecular_data/collisional_rates.html

⁵ <http://basecol.obspm.fr>

⁶ Grenoble Image and Line Data Analysis Software is provided and actively developed by IRAM, and is available at <http://www.iram.fr/IRAMFR/GILDAS>

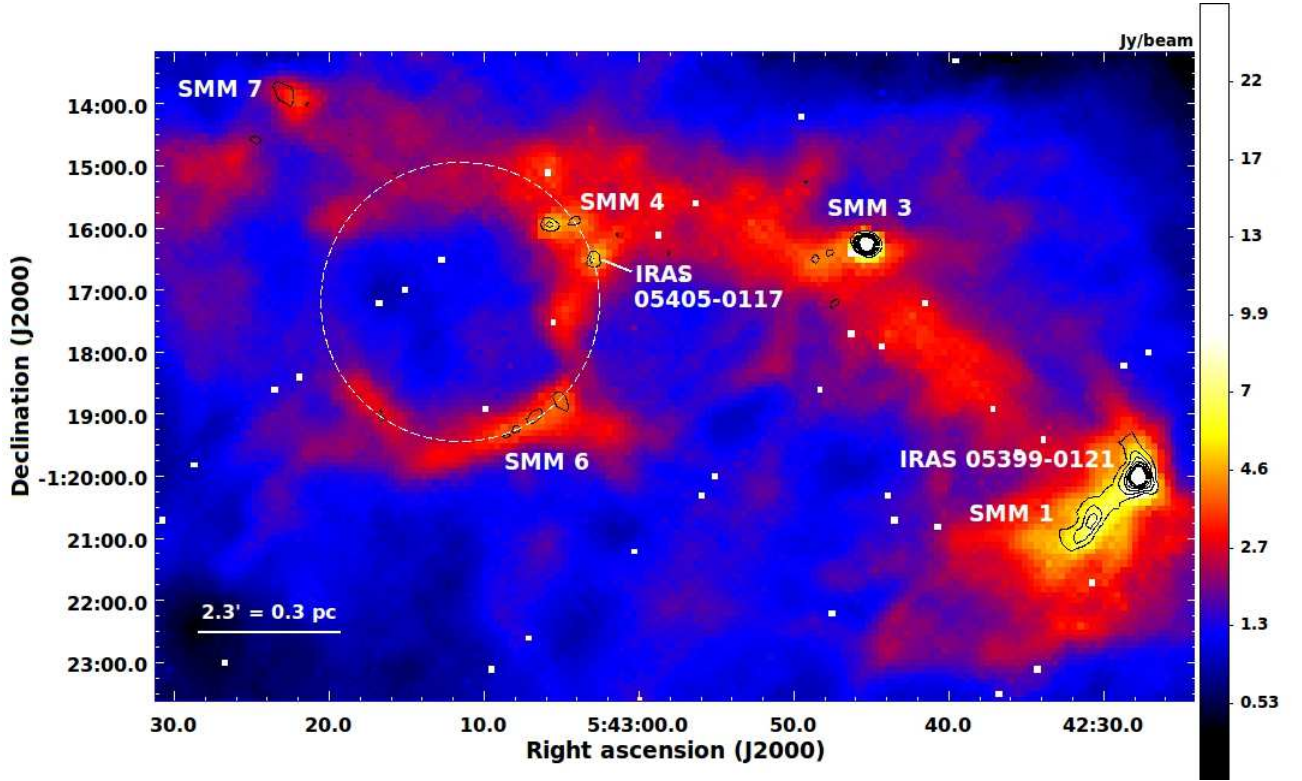


Fig. 2. *Herschel*/SPIRE 250- μm far-infrared image towards the Orion B9 star-forming filament. The image is shown with a square-root scaling to improve the contrast between bright and faint features. The image is overlaid with black contours of SABOCA 350- μm emission. The SABOCA contours start at 3σ and increase at this interval (Paper III). The SABOCA data towards the IRAS 05399/SMM 1 -system with a 1σ noise level of 80 mJy beam^{-1} are taken from Miettinen & Offner (2013). Selected cores are labelled. The ring-like structure comprising partly of SMM 6 is highlighted with a white dashed circle of radius $2.25''$ or $\sim 0.3 \text{ pc}$. A scale bar indicating the 0.3 pc projected length is shown in the bottom left corner.

Table 1. The 350- μm condensations within SMM 6.

Source	$\alpha_{2000.0}$ [h:m:s]	$\delta_{2000.0}$ [$^{\circ}$: $'$: $''$]	R_{eff} [pc]	M [M_{\odot}]	$N(\text{H}_2)$ [10^{22} cm^{-2}]	$\langle n(\text{H}_2) \rangle$ [10^5 cm^{-3}]
SMM 6a ^a	05 43 05.0	-01 18 49.3	0.02	0.6 ± 0.2	2.7 ± 1.3	3.4 ± 1.1
SMM 6b	05 43 06.8	-01 19 02.8	0.02	0.3 ± 0.1	2.2 ± 0.8	1.7 ± 0.6
SMM 6c	05 43 08.0	-01 19 13.2	0.005^b	0.1 ± 0.05^b	1.7 ± 0.7	37 ± 18^b
SMM 6d	05 43 08.6	-01 19 22.3	0.005^b	0.1 ± 0.05^b	1.9 ± 0.7	37 ± 18^b
SMM 6c+6d ^b	0.01^b	0.2 ± 0.1^b	...	9.1 ± 4.6^b

Notes. Columns (2) and (3) give the equatorial coordinates [$(\alpha, \delta)_{2000.0}$] of the SABOCA peak position. Columns (4)–(7) list, respectively, the effective radius, mass, beam-averaged peak H_2 column density, and the volume-averaged H_2 number density. The latter three are revised from those presented in Paper III (see Appendix A for details).^(a) SMM 6a was called SMM 6 in Paper III. It is renamed here for clarity because we call the parent core SMM 6.^(b) With the *clumpfind* (Williams et al. 1994) settings used in Paper III, SMM 6c and 6d were treated as a single source. The values of R_{eff} , M , and $\langle n(\text{H}_2) \rangle$ given in the last row of the table include contributions from both condensations. Approximately half of the reported size and mass of SMM 6c+6d can be assigned to both fragments, making their densities about four times the common value ($\sim 3.7 \pm 1.8 \times 10^6 \text{ cm}^{-3}$).

together and thus the total optical thickness could not be reliably determined from the sum of the peak optical thicknesses of the components. For the rest frequencies of the hf components, we used the values from Ladd et al. (1998; Table 6 therein). The adopted central frequency, $224\,714.199 \text{ MHz}$, refers to the strongest hf component $J_F = 2_{9/2} \rightarrow 1_{7/2}$ which has a relative intensity of $R_i = \frac{1}{3}$.

The $J = 3 - 2$ transition of both N_2H^+ and N_2D^+ is split up into 38 hf components spread over about 5.7 and 6.9 km s^{-1} , respectively. To fit these hf structures, we used the rest frequencies from Pagani et al. (2009; Tables 4 and 10 therein). The adopted

central frequencies of $\text{N}_2\text{H}^+(3-2)$ and $\text{N}_2\text{D}^+(3-2)$, $279\,511.832$ and $231\,321.912 \text{ MHz}$, are those of the $J_{F_1F} = 3_{45} \rightarrow 2_{34}$ hf component which has a relative intensity of $R_i = \frac{11}{63}$. Also in these cases, the hf components are blended and thus the optical thickness could not be reliably determined through hf fitting.

Table 2. Observed spectral-line transitions and observational parameters.

Transition	ν [MHz]	E_u/k_B [K]	n_{crit} [cm ⁻³]	HPBW [′′]	η_{MB}	T_{sys} [K]	PWV [mm]	Channel spacing ^a [kHz] [km s ⁻¹]	τ_{int} [min]	rms [mK]
C ¹⁷ O(2–1)	224 714.199 ^b	16.2	2.1×10^4	27.8	0.75	168–208	1.0–2.1	76.3 0.1	9	27–34
N ₂ D ⁺ (3–2)	231 321.912 ^c	22.2	3.0×10^6	27.0	0.75	204–228	1.0–2.1	76.3 0.1	9–15	30–36
N ₂ H ⁺ (3–2)	279 511.832 ^c	26.8	5.2×10^6	22.3	0.74	161–164	~ 0.2	76.3 0.08	4.2–4.8	38–41

Notes. Columns (2)–(4) give the rest frequencies of the observed transitions (ν), their upper-state energies (E_u/k_B , where k_B is the Boltzmann constant), and critical densities (see text for details). Columns (5)–(12) give the APEX beamsize (HPBW) and the main-beam efficiency (η_{MB}) at the observed frequencies, the SSB system temperatures during the observations (T_{sys} on a T_{MB} scale, see text), the amount of PWV, channel widths (both in kHz and km s⁻¹) of the original data, the on-source integration times per position (τ_{int}), and the 1σ rms noise levels at the smoothed resolution.

^(a) The original channel spacings. The final spectra were Hanning-smoothed which divides the number of channels by two. ^(b) From Ladd et al. (1998). ^(c) From Pagani et al. (2009).

3. Observational results

3.1. Spectra

The Hanning-smoothed spectra are presented in Fig. 3. The lines are clearly detected towards all condensations. The hf structure of the C¹⁷O(2–1) line is partially resolved in SMM 6b–d (note the hf satellites on the low-velocity side of the strongest component), but not sufficiently well to derive the line optical thickness. Towards SMM 6c, the C¹⁷O and N₂H⁺ lines exhibit two well-separated velocity components: besides the lines at the systemic velocity ~ 9.4 km s⁻¹, there are weak lines at a lower velocity (~ 2.3 km s⁻¹). There is also a hint of low-velocity C¹⁷O emission in the spectra towards SMM 6a and 6b. The low-velocity line emission was already detected towards other Orion B9 cores in Papers I–III and by Miettinen (2012b). We note that some of the spectra show small artificial “absorption”-like features, most notably the C¹⁷O spectra towards SMM 6a and 6b. These are caused by emission in the OFF-source reference position (OFF-beam); for example, there is C¹⁷O emission in the velocity range $\sim 1 - 2$ km s⁻¹ towards the OFF-position of SMM 6b. We also note that the nearby condensations SMM 6c and 6d are encompassed by the 22′.3–27′.8 beams. Therefore, line emission from one of the sources is (partly) caught in the beam when observing towards the dust peak of the other and may thus affect the line profiles to some degree.

3.2. Spectral-line parameters

The spectral-line parameters are listed in Table 3. The values of v_{LSR} and Δv were derived through fitting the hf structure. The quoted uncertainties are formal 1σ fitting errors. The fact that the lines are only marginally resolved at best means that the quoted Δv values represent only an upper limit to the intrinsic linewidth. The peak intensities (T_{MB}) were derived by fitting a single Gaussian to the profile of the strongest line. The integrated line intensities ($\int T_{\text{MB}} d\nu$) listed in Col. (6) of Table 3 were computed over the velocity range given in square brackets in the corresponding column. This way, we were able to take the non-Gaussian shape of the lines into account. The uncertainties in the peak and integrated intensities represent the quadrature sums of the fitting errors and the 10% calibration uncertainties. In the last two columns of Table 3, we list the estimated peak line optical-thicknesses (τ_0) and assumed excitation temperatures (T_{ex}), which are described in Sect 4.5.

4. Analysis and results

4.1. Revisiting the core fragmentation

Because the mass of the parent core is revised in the present work (Appendix A), we also re-analyse its fragmentation here.

The line mass of SMM 6 is found to be $M_{\text{line}} \simeq 27 \pm 6 M_{\odot} \text{ pc}^{-1}$. For an infinite, unmagnetised, isothermal cylinder, instability (collapse to line singularity) occurs if its M_{line} exceeds the critical equilibrium value of (e.g., Ostriker 1964; Inutsuka & Miyama 1992)

$$M_{\text{line}}^{\text{crit}} = \frac{2c_s^2}{G}, \quad (1)$$

where c_s is the isothermal sound speed and G the gravitational constant. Using the gas temperature $T_{\text{kin}} = 11.0 \pm 0.4$ K to calculate the sound speed (0.196 ± 0.004 km s⁻¹), we derive the value $M_{\text{line}}^{\text{crit}} = 17.8 \pm 0.6 M_{\odot} \text{ pc}^{-1}$. If the ~ 0.1 km s⁻¹ non-thermal velocity dispersion derived in Paper II is taken into account, the effective sound speed $c_{\text{eff}} = (c_s^2 + \sigma_{\text{NT}}^2)^{1/2}$ increases the value of $M_{\text{line}}^{\text{crit}}$ to $\sim 22.5 \pm 0.8 M_{\odot} \text{ pc}^{-1}$. SMM 6 therefore appears to be (slightly) supercritical, in accordance with the detected substructure along the filament.

The projected spacing between the condensations is $\sim 29''$ or ~ 0.06 pc, where the sources 6c and 6d are treated as a single fragment. In the case the cylinder has $M_{\text{line}} = M_{\text{line}}^{\text{crit}}$ as is roughly the case for SMM 6, the Jeans length along the long axis is (Larson 1985; Hartmann 2002)

$$\lambda_J^{\text{cyl}} = \frac{3.94c_s^2}{G\Sigma_0}, \quad (2)$$

where $\Sigma_0 = \mu_{\text{H}_2} m_{\text{H}} N(\text{H}_2)$ is the central surface density with $\mu_{\text{H}_2} = 2.82$ being the mean molecular weight per H₂ molecule (when the He/H abundance ratio is about 0.1; see Appendix A) and m_{H} the mass of a hydrogen atom. If the central column density is adopted to be the average value derived towards the condensations, $\sim 2.1 \pm 0.2 \times 10^{22}$ cm⁻² [Col. (6) of Table 1], λ_J^{cyl} is $\simeq 0.07 \pm 0.01$ pc – very close to the observed interval of the condensations. We note that due to projection effects we are measuring only a lower limit to the separations.

If the *finite* length and diameter of the cylindrical cloud are L and D , respectively, the number of fragments forming due to gravitational instability is expected to be (e.g., Bastien et al. 1991; Wiseman & Ho 1998)

$$N_{\text{frag}} = \frac{L}{\lambda_{\text{crit}}} = \frac{2(L/D)}{3.94} \simeq 0.5A, \quad (3)$$

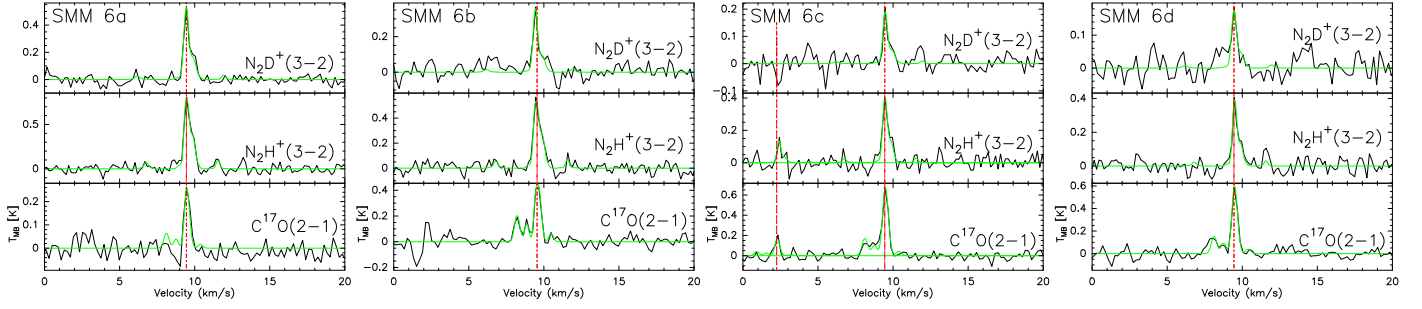


Fig. 3. Hanning-smoothed $C^{17}O(2-1)$, $N_2H^+(3-2)$, and $N_2D^+(3-2)$ spectra. Hyperfine-structure fits to the lines are overlaid in green. In each panel, the vertical red dashed line indicates the radial velocity of the $C^{17}O(2-1)$ line. Note that towards SMM 6c, two velocity components of $C^{17}O(2-1)$ and $N_2H^+(3-2)$ (at ~ 2.3 and ~ 9.4 km s^{-1}) are detected.

Table 3. Spectral-line parameters.

Source	Transition	v_{LSR} [km s^{-1}]	Δv [km s^{-1}]	T_{MB} [K]	$\int T_{\text{MB}} dv^a$ [K km s^{-1}]	τ_0^b	T_{ex}^c [K]
SMM 6a	$C^{17}O(2-1)$	9.45 ± 0.02	0.36 ± 0.05	0.28 ± 0.05	0.12 ± 0.02 [9.09, 10.46; 73.4%]	0.05 ± 0.01	10.0
	$N_2H^+(3-2)$	9.42 ± 0.01	0.27 ± 0.02	0.71 ± 0.11	0.56 ± 0.06 [6.26, 12.00; 99.9%]	1.62 ± 0.28	5.0
SMM 6b	$N_2D^+(3-2)$	9.38 ± 0.01	0.33 ± 0.01	0.47 ± 0.10	0.30 ± 0.04 [8.22, 11.09; 92.6%]	0.52 ± 0.04	5.0
	$C^{17}O(2-1)$	9.55 ± 0.02	0.34 ± 0.02	0.48 ± 0.06	0.39 ± 0.05 [7.69, 10.74; 100%]	0.09 ± 0.01	10.0
	$N_2H^+(3-2)$	9.44 ± 0.01	0.27 ± 0.03	0.49 ± 0.08	0.37 ± 0.04 [7.90, 10.67; 92.6%]	0.81 ± 0.06	5.0
SMM 6c	$N_2D^+(3-2)$	9.38 ± 0.02	0.33 ± 0.04	0.35 ± 0.05	0.21 ± 0.03 [8.46, 10.67; 92.6%]	0.36 ± 0.01	5.0
	$C^{17}O(2-1)$	9.45 ± 0.01	0.42 ± 0.03	0.68 ± 0.08	0.46 ± 0.05 [7.66, 10.42; 100%]	0.14 ± 0.01	10.0
SMM 6c (2nd v-comp.)	$C^{17}O(2-1)$	2.25 ± 0.10	0.34 ± 0.29	0.21 ± 0.02	0.06 ± 0.04 [1.50, 2.79; 78.7%]	0.04 ± 0.01	10.0
	$N_2H^+(3-2)$	9.41 ± 0.02	0.27 ± 0.04	0.34 ± 0.06	0.23 ± 0.03 [8.57, 11.72; 96.1%]	0.48 ± 0.02	5.0
SMM 6c (2nd v-comp.)	$N_2H^+(3-2)$	2.36 ± 0.03	0.27 ± 0.03	0.16 ± 0.05	0.05 ± 0.01 [1.92, 3.04; 89.9%]	0.20 ± 0.01	5.0
	$N_2D^+(3-2)$	9.42 ± 0.03	0.33 ± 0.02	0.21 ± 0.02	0.10 ± 0.02 [8.53, 10.32; 90.9%]	0.20 ± 0.01	5.0
SMM 6d	$C^{17}O(2-1)$	9.45 ± 0.01	0.39 ± 0.03	0.60 ± 0.06	0.42 ± 0.05 [6.82, 10.98; 100%]	0.12 ± 0.01	10.0
	$N_2H^+(3-2)$	9.45 ± 0.01	0.27 ± 0.02	0.32 ± 0.07	0.26 ± 0.03 [8.22, 12.03; 96.2%]	0.45 ± 0.03	5.0
	$N_2D^+(3-2)$	9.38 ± 0.04	0.35 ± 0.11	0.17 ± 0.02	0.14 ± 0.04 [7.73, 10.53; 87.2%]	0.16 ± 0.01	5.0

Notes. ^(a) Integrated intensity was computed by integrating over the velocity range indicated in square brackets (in km s^{-1}). The percentage value indicates the contribution of hf components' intensity lying within the corresponding velocity range. ^(b) The optical thickness in the centre of the strongest hf component; it was derived using the assumed T_{ex} value given in the last column. ^(c) T_{ex} is assumed to be the same for the $J = 3 - 2$ transition of N_2H^+ and N_2D^+ . See Sect. 4.5 for details.

where $\lambda_{\text{crit}} = 1.97D$ is the wavelength of the most unstable perturbation, and A the cylinder's aspect ratio. The average width of the SMM 6 filament is about $26''.4$ or $D = 2R = 0.06$ pc, so A is about 4. One would therefore expect to have two subfragments, i.e., half the number we observe. The discrepancy could be caused by projection effects (the true length of the filament is longer), and the fact that the source is not a perfect cylinder but is bent or curved as shown in Fig. 2 and it narrows towards the southeast (i.e., D is changing along the filament). The number of detected subfragments could also be an imprint of internal turbulent motions, i.e., turbulent fragmentation (cf. Nakamura et al. 2012). Note that λ_{crit} is about 0.12 pc when computed using the average width 0.06 pc, i.e., a factor of 1.7 larger than λ_J^{cyl} .

We conclude that SMM 6 has likely fragmented into subcondensations as a result of cylindrical Jeans-type gravitational instability. Considering a filament of radius R , the fragmentation timescale is then expected to be comparable to the radial crossing time, $\tau_{\text{cross}} = R/\sigma$, where σ refers to the total velocity dispersion. If we use the average FWHM linewidth of the $C^{17}O$ lines detected here, $\Delta v = \sqrt{8 \ln 2} \sigma = 0.38$ km s^{-1} , the τ_{cross} for the SMM 6 filament is $\sim 1.8 \times 10^5$ yr.

4.2. Gas velocity dispersion and virial state of the condensations

To study the gas kinematics of the high-density portion of the condensations, we employed the $N_2H^+(3-2)$ transition due to its high critical density. We computed the non-thermal portion of the line-of-sight velocity dispersion, σ_{NT} , using Eq. (9) of Paper II. It was assumed that $T_{\text{kin}} = 10$ K, and the error in σ_{NT} was calculated from that of the FWHM linewidth. As shown in Col. (2) of Table 4, $\sigma_{\text{NT}} = 0.1$ km s^{-1} for each source. Because the isothermal sound speed at 10 K is $c_s = 0.19$ km s^{-1} , the σ_{NT}/c_s ratios are $\sim 0.5 \pm 0.1$, i.e., the condensations are characterised by *subsonic* internal non-thermal (turbulent) motions. The true values of σ_{NT} could be even lower because the $N_2H^+(3-2)$ lines are not spectrally resolved, enabling us to derive only upper limits to the linewidths and velocity dispersions.

To examine the dynamical state of the condensations, we calculated their virial masses by employing the $N_2H^+(3-2)$ linewidths and using the formula where the effects of external pressure, rotation, and magnetic field are ignored [cf. Eq. (12) of Paper II]:

$$M_{\text{vir}} = \frac{5}{8 \ln 2} \frac{R_{\text{eff}} \Delta v^2}{aG}, \quad (4)$$

Table 4. The one-dimensional non-thermal velocity dispersions, virial masses, and virial parameters of the condensations.

Source	σ_{NT} [km s ⁻¹]	M_{vir}^a [M _⊙]	α_{vir}
SMM 6a	0.10 ± 0.01	0.6 ± 0.03	1.0 ± 0.4
SMM 6b	0.10 ± 0.01	0.6 ± 0.04	2.1 ± 0.7
SMM 6c	0.10 ± 0.02	0.16 ± 0.01 ^b	1.6 ± 0.8 ^b
SMM 6d	0.10 ± 0.01	0.16 ± 0.01 ^b	1.6 ± 0.8 ^b
SMM 6c+6d	...	0.3 ± 0.02 ^c	1.6 ± 0.8 ^c

Notes. The listed values assume that $T_{\text{kin}} = 10$ K.^(a) A density profile that declines like $\sim r^{-2}$ was assumed.^(b) These values assume that the radii and masses of SMM 6c and 6d are ~ 0.005 pc and ~ 0.1 M_⊙ (cf. Table 1).^(c) For these values SMM 6c and 6d are treated as a one source.

where the dimensionless parameter a measures the effect of a non-uniform density distribution on the gravitational energy and is given by $a = (1 - p/3)/(1 - 2p/5)$, where p is the power-law index of the density profile ($n \propto r^{-p}$; Bertoldi & McKee 1992). Following ABMP07, we assume that the density structure of the sources is that of a centrally condensed isothermal sphere with $n(r) \propto r^{-2}$ ($a = 5/3$). The resulting values are listed in Col. (3) of Table 4 with uncertainties propagated from the linewidth errors. We note that if the condensations have inner density profiles shallower than $\sim r^{-2}$, the virial masses will be higher. For example, if the density power-law index is $p = 1$ or $a = 10/9$, the M_{vir} values are larger by a factor of 1.5 compared to those with $p = 2$.

The virial parameters of the condensations were calculated following the definition by Bertoldi & McKee (1992), i.e., $\alpha_{\text{vir}} = M_{\text{vir}}/M$. The values are given in Col. (4) of Table 4 with the uncertainties derived by propagating the errors in both mass estimates. The uncertainties in α_{vir} are quite large, but gravitational boundedness with $\alpha_{\text{vir}} < 2$ seems possible at least for SMM 6a and 6c,d. If the intrinsic N₂H⁺(3–2) linewidths are smaller, the α_{vir} values would also become smaller enhancing the importance of the condensations’ self-gravity.

4.3. Relative motions and interactions between the condensations

The centroid velocity difference between C¹⁷O and N₂H⁺ for each condensation is small, only 0.045 km s⁻¹ on average. This suggests that the condensations are not moving much with respect to the lower-density envelope (e.g., Kirk et al. 2007, 2010). The observed radial velocity data can also be used to study the (possible) motions of the condensations relative to one another (e.g., ABMP07). The average line-of-sight or radial velocity of the N₂H⁺(3–2) lines is 9.43 km s⁻¹ and the dispersion of the velocity centroids is $\sigma_{\text{VLSR}, 1\text{D}}^{\text{N}_2\text{H}^+} \approx 0.02$ km s⁻¹ ($\langle v_{\text{LSR}} \rangle = 9.48$ km s⁻¹ and $\sigma_{\text{VLSR}, 1\text{D}}^{\text{C}^{17}\text{O}} \approx 0.05$ km s⁻¹ for the optically thin C¹⁷O lines). The latter value is taken to represent the one-dimensional dispersion of the velocities of the high-density condensations (Peng et al. 1998; ABMP07). If the condensation velocities perpendicular to the line of sight are the same as their radial velocities, the three-dimensional dispersion of the velocities would be $\sigma_{3\text{D}}^{\text{N}_2\text{H}^+} = \sqrt{3} \times \sigma_{\text{VLSR}, 1\text{D}}^{\text{N}_2\text{H}^+} \approx 0.03$ km s⁻¹. If the orientation of the SMM 6 filament is *not* exactly perpendicular to our line of sight, and *if* the condensations would be moving along the filament, one would expect to see an imprint of these motions in the radial velocity data. The v_{LSR} values would be expected to change

monotonically if the movement of condensations along the parent filament (in either direction) is taking place. However, such a systematic trend is not observed.

As mentioned in Appendix A the length of SMM 6 along its long axis is $L = 0.22$ pc. Using the above value of $\sigma_{3\text{D}}^{\text{N}_2\text{H}^+}$, a typical timescale for the condensations to cross the long axis of the parent core becomes $\tau_{\text{cross}}^{\text{long}} = L/\sigma_{3\text{D}}^{\text{N}_2\text{H}^+} \approx 7.2 \times 10^6$ yr. On the other hand, the average width of the filament, $D = 2R = 0.06$ pc, suggests a radial crossing time of $\tau_{\text{cross}}^{\text{radial}} = D/\sigma_{3\text{D}}^{\text{N}_2\text{H}^+} \approx 2 \times 10^6$ yr. Because the projected separation between the condensations is also ≈ 0.06 pc (when SMM 6c and 6d are treated as a one fragmentation), the time required for one condensation to encounter and interact with another condensation is expected to be ~ 2 Myr (e.g., Takakuwa et al. 2003). We note that there are two effects that can affect the rate of collision between condensations: *i*) gas drag caused by the surrounding medium, and *ii*) gravitational focusing (ABMP07). While the former is likely to make the real collision timescale longer, the latter could enhance the collision rate. Moreover, gas gradients (density, velocity) in the parent filament (cf. Kirk et al. 2013) could modify the time required for the condensations to encounter and interact with one another.

If the representative density of the condensations is $\sim a$ few $\times 10^5$ cm⁻³, their free-fall time is only $\tau_{\text{ff}} \sim 7 \times 10^4$ yr. Therefore, it seems unlikely that the condensations have time to interact with one another before collapsing into protostars or proto-brown dwarfs unless their lifetime is a few tens of τ_{ff} , which seems unlikely (see, e.g., ABMP07, and references therein). Within the errors, it is in principle possible that the condensations are not gravitationally bound. For unbound condensations, one should also consider the dissipation timescale, $\tau_{\text{diss}} = 2R_{\text{eff}}/c_{\text{eff}}$ (e.g., Takakuwa et al. 2003). For the average condensation effective radius, 0.017 pc, and average c_{eff} calculated from the N₂H⁺(3–2) lines, 0.215 km s⁻¹, τ_{diss} becomes $\sim 1.5 \times 10^5$ yr. The typical dissipation speed of the condensations would therefore be an order of magnitude shorter than the coalescence timescale.

4.4. Mass accretion onto the condensations

Some numerical simulations suggest that protostars can gain mass via competitive accretion, i.e., accretion from a shared reservoir of material (Bonnell et al. 2001; Bonnell & Bate 2006). Even though competitive accretion models apply to protostars that accrete the available gas while moving around within the protocluster potential well, we can still obtain a rough estimate of the accretion rate onto the starless condensations if competitive-like accretion is occurring (cf. ABMP07). The mass accretion rate is given by $\dot{M}_{\text{acc}} \approx \pi \rho_0 V_{\text{rel}} R_{\text{acc}}^2$, where ρ_0 is the gas density of the background medium, V_{rel} is the relative velocity of the subfragments with respect to the ambient medium, and R_{acc} is the accretion radius [see Eq. (3) of ABMP07]. The revised volume-average density of SMM 6 is about $\sim 1.6 \times 10^4$ cm⁻³, the value we adopt for the background gas density. We assume that V_{rel} is equal to $\sigma_{3\text{D}}^{\text{N}_2\text{H}^+} \approx 0.03$ km s⁻¹.⁷ As concluded by ABMP07, R_{acc} is typically comparable to the condensation radius, and

⁷ ABMP07 assumed that the velocity distribution of their sample of condensations was given by the Maxwell-Boltzmann distribution, and adopted V_{rel} for the average relative speed of a condensation ($v_{\text{ave}} = \sqrt{8/\pi} \times \sigma_{\text{VLSR}, 1\text{D}}^{\text{N}_2\text{H}^+}$ in our notation). The Maxwell-Boltzmann distribution is not expected to apply to our small number of subfragments, but we note that the value of $\sigma_{3\text{D}}^{\text{N}_2\text{H}^+}$ is very close to v_{ave} .

therefore we estimate it to be the average effective radius of the condensations, i.e., 0.017 pc. We thus derive the value $\dot{M}_{\text{acc}} \sim 2.6 \times 10^{-8} M_{\odot} \text{ yr}^{-1}$. For comparison, the characteristic mass infall rate for a singular isothermal sphere undergoing gravitational collapse, $\sim c_s^3/G$ (Shu 1977), is $\sim 1.5 \times 10^{-6} M_{\odot} \text{ yr}^{-1}$ at 10 K – about 60 times higher than the above \dot{M}_{acc} value. Local gravitational instability of the individual condensations is therefore likely to be more important than competitive-like accretion (ABMP07). However, given the total mass of the parent core, $5.9 \pm 1.3 M_{\odot}$, there is a considerable mass reservoir for (some of) the condensations to increase their mass via accretion, although by how much remains unclear. High-resolution spectral-line imaging of the whole core would be necessary to study whether there are infall motions towards the condensations and to estimate how much additional mass they could accrete (cf. Hacar & Tafalla 2011).

4.5. Molecular column densities and fractional abundances

To properly determine the column density of the molecules, we must first determine the optical thickness of the transition. The optical thickness of a spectral line can be derived from the radiative transfer equation, provided the line intensity and excitation temperature are known (as mentioned in Sect. 2, the optical thickness could not be derived through fitting the hf structure). We used the line peak intensities (T_{MB}) to calculate the peak optical thicknesses, τ_0 [see, e.g., Eq. (A.3) in Miettinen 2012a]. The $\text{C}^{17}\text{O}(2-1)$ transition was assumed to be thermalised at the adopted gas temperature of the condensations, i.e., we set $T_{\text{ex}} = 10$ K. This assumption is supported by the results obtained in Paper III [$T_{\text{ex}}(\text{C}^{17}\text{O}) \simeq T_{\text{kin}}$]. For the $J = 3-2$ transition of N_2H^+ and N_2D^+ , we adopted the value $T_{\text{ex}} = 5$ K. This is the typical value derived for the $J = 3-2$ line or lower- J lines of N_2H^+ and N_2D^+ (e.g., Caselli et al. 2002; Crapsi et al. 2005; Papers II–III; Friesen et al. 2013). Finally, the background temperature was assumed to be equal to the cosmic background radiation temperature of 2.725 K. The derived τ_0 values are listed in Col. (7) of Table 3, with the uncertainties propagated from those in T_{MB} .

The beam-averaged C^{17}O column densities, $N(\text{C}^{17}\text{O})$, were derived following the standard LTE analysis outlined, e.g., in the paper by Miettinen (2012a; Appendix A.3 therein). Because the τ_0 values of the C^{17}O lines are so small, even the total optical thicknesses are $\tau_{\text{tot}} \ll 1$ (as seen in a number of other studies; e.g., Ladd et al. 1998; Fuller & Ladd 2002). The $N(\text{C}^{17}\text{O})$ values were therefore computed from the integrated line intensities under the assumption of optically thin line emission. In the two cases where the detected line does not cover all the hf components (SMM 6a and 2nd velocity component towards SMM 6c), the column density was scaled by the inverse of the relative line strength within the detected line. The errors in $N(\text{C}^{17}\text{O})$ were propagated from those associated with the integrated intensity.

Because the strongest hf component of the $J = 3-2$ transition of N_2H^+ and N_2D^+ has a relative strength of only $11/63 = 0.1746$, the τ_{tot} values inferred from τ_0 are clearly above unity in most cases, i.e., the lines are optically thick (as is often the case for these lines; e.g., Crapsi et al. 2004; Fontani et al. 2006). The beam-averaged column densities of N_2H^+ and N_2D^+ were therefore computed from the FWHM linewidths and τ_{tot} [see, e.g., Eq. (10) in Paper II]. The column density uncertainties were derived from those of Δv and τ_{tot} . If we are overestimating the true linewidths, the corresponding column densities would represent upper limits in this sense. We also checked our derivation of the column density by examining some additional optically

thin hf satellites. The N_2H^+ line towards SMM 6a offered the best opportunity to do this because in this case five hf lines lying 1.5–2.4 km s⁻¹ from the strongest component were clearly detected (Fig. 3). The integrated intensity of the satellite group is 0.05 ± 0.04 K km s⁻¹ and its overall relative strength is about 0.035. These can be converted into a total $N(\text{N}_2\text{H}^+)$ of $1.5 \pm 1.2 \times 10^{13}$ cm⁻², which is 0.6 ± 0.5 times the value derived from τ_{tot} . The results are in reasonable agreement within the error.

The fractional abundances of the molecules were calculated by dividing their column densities by the H_2 column density. For this purpose, the $N(\text{H}_2)$ values were derived from the SABOCA map smoothed to the corresponding resolution of the line observations. The abundance errors were derived by propagating the errors in the column densities of the observed species and H_2 molecules. The derived column densities and abundances are listed in Table 5.

4.6. CO depletion and deuterium fractionation

To investigate the amount of CO depletion in the condensations, we calculated the CO depletion factors following the analysis presented in Sect. 4.5 of Paper III. In summary, the canonical (or undepleted) CO abundance was adopted to be 9.5×10^{-5} (Frerking et al. 1982). With the additional assumptions about the oxygen-isotopic ratios, namely $[\text{C}^{16}\text{O}]/[\text{C}^{18}\text{O}] = 500$ and $[\text{C}^{18}\text{O}]/[\text{C}^{17}\text{O}] = 3.52$, the canonical C^{17}O abundance was set to 5.4×10^{-8} . This value was then divided by the observed C^{17}O abundance, which gives the CO depletion factor, f_{D} (the eighth column of Table 5). The f_{D} uncertainty was propagated from that in the observed abundance but it probably underestimates the true uncertainty by a factor of 2–3 because of the uncertainties in the assumptions used (e.g., canonical abundance, oxygen-isotopic ratios, etc.). For instance, Lacey et al. (1994) found the best-fitting CO abundance of $2.7_{-1.2}^{+6.4} \times 10^{-4}$ towards NGC 2024 in Orion B. Adopting this value would almost triple our f_{D} values. A lower limit to the condensation’s age can be estimated to be comparable to its CO depletion timescale. Following the analysis presented in Miettinen (2012a, Sect. 5.5 therein), at a characteristic density of a few times 10^5 cm⁻³, the depletion time is $\tau_{\text{dep}} \sim 2.2 \times 10^4$ yr.

Towards each condensation, the N_2H^+ and N_2D^+ lines have similar radial velocities and linewidths. Therefore, the two lines are probably tracing the same gas. It is therefore reasonable to calculate the degree of deuterium fractionation by dividing the column density of the deuterated isotopologue N_2D^+ by its normal hydrogen-bearing form N_2H^+ . The error was derived from the errors in the corresponding column densities. The results are shown in the last column of Table 5.

5. Discussion

5.1. Substructure within Ori B9–SMM 6

The studied core SMM 6 is one of the rare examples of a prestellar core that is fragmented into smaller condensations. Even though the theoretical predictions of the cylindrical fragmentation are not exactly similar to the observed characteristics, it still seems likely that the core has fragmented as a result of Jeans-type gravitational instability. In particular, the projected separation between the fragments is very close to the local thermal Jeans length. The radial crossing time of the filamentary parent core suggests that its fragmentation timescale is ~ 0.18 Myr.

Table 5. Molecular column densities, fractional abundances with respect to H₂, CO depletion factors, and the deuteration degrees.

Source	$N(\text{C}^{17}\text{O})$ [10 ¹⁴ cm ⁻²]	$N(\text{N}_2\text{H}^+)$ [10 ¹³ cm ⁻²]	$N(\text{N}_2\text{D}^+)$ [10 ¹² cm ⁻²]	$x(\text{C}^{17}\text{O})$ [10 ⁻⁸]	$x(\text{N}_2\text{H}^+)$ [10 ⁻⁹]	$x(\text{N}_2\text{D}^+)$ [10 ⁻¹⁰]	f_{D}	$N(\text{N}_2\text{D}^+)/N(\text{N}_2\text{H}^+)$
SMM 6a	1.1 ± 0.2	2.5 ± 0.5 ^a	7.6 ± 0.6	1.5 ± 0.6	2.3 ± 0.9	9.9 ± 3.5	3.6 ± 1.5	0.30 ± 0.07
SMM 6b	2.5 ± 0.3	1.2 ± 0.2	5.2 ± 0.7	3.5 ± 1.4	1.3 ± 0.5	7.2 ± 2.8	1.5 ± 0.6	0.43 ± 0.09
SMM 6c	3.0 ± 0.3	0.7 ± 0.1	2.9 ± 0.2	5.4 ± 2.2	0.9 ± 0.4	4.9 ± 1.9	1.0 ± 0.4	0.41 ± 0.07
SMM 6c (2nd v-comp.)	0.5 ± 0.3	0.3 ± 0.1	...	0.9 ± 0.6	0.4 ± 0.1	...	5.9 ± 4.1	...
SMM 6d	2.7 ± 0.3	0.7 ± 0.1	2.5 ± 0.8	6.4 ± 3.1	1.1 ± 0.5	5.5 ± 3.0	0.8 ± 0.4	0.36 ± 0.13

Notes. The $N(\text{C}^{17}\text{O})$ values were computed by assuming that $T_{\text{ex}} = 10$ K. The N_2H^+ and N_2D^+ column densities were derived under the assumption that $T_{\text{ex}} = 5$ K.^(a) The value derived from a group of five optically thin satellites is $1.5 \pm 1.2 \times 10^{13}$ cm⁻² (see text).

The estimated masses of the condensations are $\sim 0.2 - 0.6 M_{\odot}$ with a typical uncertainty of $\sim 0.1 M_{\odot}$. The condensations are characterised by subsonic non-thermal motions with $\sigma_{\text{NT}} \simeq 0.5c_s$ assuming that the characteristic gas temperature is 10 K. The calculated condensation virial parameters have relatively large errors, but it seems likely that they are self-gravitating. The minimum mass for a main-sequence star is $M_{\star} = 0.08 M_{\odot}$, below which the stellar temperature is not high enough to ignite proton-proton nuclear fusion. If the star formation efficiency for individual condensations is comparable to that of dense cores, $\epsilon_{\text{core}} = M_{\star}/M_{\text{core}} \sim 30 - 50\%$ (e.g., Matzner & McKee 2000; Goodwin et al. 2008; André et al. 2009), they might be able to collapse to form stars without any additional mass accretion. At least for the most massive fragment, SMM 6a, this seems possible. The lowest mass fragments could also form substellar-mass objects or brown dwarfs ($0.012 < M/M_{\odot} < 0.08$; e.g., Mollière & Mordasini 2012). Examples of brown dwarfs that were likely formed or are currently forming via direct collapse include the wide (800 AU) binary brown dwarf system FU Tau A/B (Luhman et al. 2009) and the pre-brown dwarf condensation Oph B-11 discovered by André et al. (2012). Some of the very low luminosity objects, such as L1148-IRS, could also be the precursors of isolated brown dwarfs (Kauflmann et al. 2011). Brown dwarfs may also form (and subsequently be ejected) through disk fragmentation (see, e.g., Stamatellos & Whitworth 2009). In theory, the minimum mass of an object capable of forming through gas fragmentation is set by the opacity limit for radiative cooling and is in the range $\sim 0.001 - 0.004 M_{\odot}$, that is to say, fragmentation could even form planetary-mass objects (e.g., Whitworth & Stamatellos 2006).

The dispersion of the condensation velocity centroids is smaller than the one-dimensional velocity dispersion of the parent core gas by a factor of 11 (0.02 vs. 0.22 km s⁻¹, where the latter is derived from c_s at 11 K and 0.1 km s⁻¹ non-thermal contribution). Synthetic observations (e.g., N_2H^+) of simulated environments (decaying and driven turbulence) by Offner et al. (2008) also show that on the scale of cores, the dispersion of the velocity centroids is small (cf. Offner et al. 2009). Indeed, the motions of the condensations relative to one another appear to be so slow that they have no time to coalesce or gather together before evolving individually into protostars or proto-brown dwarfs. Moreover, despite the relatively large mass reservoir ($\sim 6 M_{\odot}$) surrounding the condensations, they are unlikely to be able to increase their mass via competitive-like accretion. Instead, the fragments' internal self-gravity could induce inward motions and accretion of additional mass – a scenario that could be tested by future high-resolution observations.

5.2. CO depletion and deuterium fractionation in the condensations

The gas phase depletion factors of CO derived towards the condensations are in the range $f_{\text{D}} = 0.8 \pm 0.4 - 3.6 \pm 1.5$. Therefore, there is no evidence of significant CO depletion. There are a few examples of high-density ($\sim 10^5$ cm⁻³) cores where CO depletion is not prominent, namely L1495B, L1521B, and L1521E (Tafalla & Santiago 2004; Hirota et al. 2004). Deuterium fractionation in these Taurus cores is also found to be low (Hirota et al. 2004, and references therein), and they are considered to be both chemically and dynamically young.

However, as mentioned in Sect. 4.6, the undepleted CO abundance in Orion B9 might well be higher than what we have adopted in the analysis. For this reason, we might be underestimating the f_{D} values by a factor of about three (Lacy et al. 1994). Also, we have observed the $J = 2 - 1$ rotational transition of C^{17}O , the line whose 10-K critical density is 2.1×10^4 cm⁻³. Apart from the condensations, we might therefore be tracing lower density gas along the line of sight where CO is not significantly depleted (e.g., Fontani et al. 2012). The 27'8 resolution of our C^{17}O observations also provides us with only beam-averaged f_{D} values. The above factors are likely to explain the f_{D} value less than unity derived for SMM 6d. Indeed, the temperatures and densities of the condensations are likely to be so low and high, respectively, that significant CO freeze-out is expected (e.g., Léger 1983; Rawlings et al. 1992). For example, Tafalla et al. (2004) estimated that the density at which CO disappears from the gas phase is only 7.8×10^4 cm⁻³ and 2.5×10^4 cm⁻³ for the starless cores L1498 and L1517B in Taurus, respectively. Moreover, for our condensations the CO freeze-out timescale is estimated to be shorter than the free-fall time by a factor of about four (see Bergin & Tafalla 2007) and about eight times shorter than the fragmentation timescale (τ_{cross}).

For comparison, Caselli et al. (1999) found that CO is depleted by a factor of ~ 10 at the dust peak of the prestellar core L1544. Similarly, Savva et al. (2003) found that, relative to the canonical abundances from Frerking et al. (1982), CO is depleted by a factor of ~ 10 in a sample of nine dense cores in Orion B. More recently, Christie et al. (2012) derived the mean (median) CO depletion factor of 19 (10) towards starless cores in the NGC 2024 region of Orion B. We note that in Paper III, where we also employed APEX/ $\text{C}^{17}\text{O}(2 - 1)$ observations, we derived the value $f_{\text{D}} = 4.2 \pm 1.3$ towards a position lying 11'' north of the 350- μm peak of SMM 6a (where we now obtain the value 3.6 ± 1.5). One would expect to see stronger depletion towards the denser dust peak, but there are two reasons that explain this discrepancy: *i*) the C^{17}O column densities in Paper III were derived through non-LTE RADEX analysis (van der Tak et al. 2007), and *ii*) the H₂ column densities were computed from the LABOCA 870- μm peak flux densities as-

suming a thick ice mantle dust model of OH94 and a dust-to-gas ratio of 1/100 (see Appendix A).

When CO molecules freeze out on the surface of dust grains, the rate of gas-phase deuterium fractionation increases (e.g., Dalgarno & Lepp 1984). The reason for this is that the main destruction path of H_2D^+ , namely $\text{H}_2\text{D}^+ + \text{CO} \rightarrow \text{HCO}^+$ or DCO^+ , is no longer effective, enabling H_2D^+ to donate its deuteron to other species (e.g., $\text{H}_2\text{D}^+ + \text{N}_2 \rightarrow \text{N}_2\text{H}^+$ or N_2D^+). The levels of $\text{N}_2\text{D}^+/\text{N}_2\text{H}^+$ deuteration we derive here, $0.30 \pm 0.07 - 0.43 \pm 0.09$, are relatively high compared to those found in other studies of starless cores. For example, Crapsi et al. (2005) found $\text{N}_2\text{D}^+/\text{N}_2\text{H}^+$ column density ratios in the range $< 0.02 - 0.44 \pm 0.08$ for their sample of starless/prestellar cores. Friesen et al. (2013) derived the values $\lesssim 0.02 - 0.20 \pm 0.04$ towards starless and protostellar cores in Perseus with no significant difference between the two types of objects. Through radiative transfer modelling of the starless core L183, Pagani et al. (2007) derived a deuteration level of 0.70 ± 0.12 at the CO-depleted core centre, exceeding the highest value found in the present study. As for f_D , a high value of deuteration (0.60 ± 0.08) was derived in Paper III towards the edge of SMM 6. Again, the column density calculations were based on RADEX analysis (N_2H^+) and LTE modelling with CLASS/Weeds (N_2D^+), and are therefore not directly comparable with the present results.

The deuterium fractionation of N_2H^+ and the amount of CO depletion are found to be positively correlated in starless/prestellar cores and the envelopes of Class 0 protostars (e.g., Crapsi et al. 2004, 2005; Emprechtinger et al. 2009). This is not evident among our condensations. In fact, the most CO-depleted fragment, SMM 6a, shows the lowest level of deuteration. Our source sample is, however, very small, and within the error bars the values of f_D and $N(\text{N}_2\text{D}^+)/N(\text{N}_2\text{H}^+)$ are comparable to each other, suggesting that they are in a similar stage of chemical and dynamical evolution. This conforms to the scenario where the condensations were formed simultaneously via core fragmentation. The high levels of molecular D/H ratio suggest that they are highly evolved, and possibly at the onset of protostellar collapse. This seems to contradict the low depletion factors in the condensations, but as discussed above we are very likely underestimating the f_D values.

6. Summary and conclusions

We have used the APEX telescope to observe the molecular-line transitions $\text{C}^{17}\text{O}(2-1)$, $\text{N}_2\text{H}^+(3-2)$, and $\text{N}_2\text{D}^+(3-2)$ towards the low-mass condensations inside the prestellar core Ori B9–SMM 6 which were discovered by our previous SABOCA 350- μm imaging of the core (Paper III). The present work is one of the first studies of the dynamics of subfragments within a prestellar core.

The condensations were likely formed as a result of Jeans-type fragmentation of the parent core. Based on the C^{17}O velocity dispersion data, we estimate that the fragmentation timescale of the filamentary parent core is $\sim 1.8 \times 10^5$ yr. The condensations show only subsonic internal non-thermal motions ($\sigma_{\text{NT}} = 0.1 \text{ km s}^{-1}$ if $T_{\text{kin}} = 10 \text{ K}$), and most of them are likely to be gravitationally bound. The condensation-to-condensation kinematics was investigated by employing the velocity information provided by the high-density tracer $\text{N}_2\text{H}^+(3-2)$. The estimated timescale required for the condensations to coalesce is a few Myr, which is much longer than their free-fall timescale. It is therefore unlikely that the subfragments will have time to coalesce before collapsing into protostars or proto-brown dwarfs, or fragment even further down to planetary-mass ob-

jects. Significant accretion in a competitive fashion between the condensations from the parent core’s mass reservoir is also unlikely. The reason for this is that the condensations’ self-gravity is expected to lead to a much higher (by a factor of ~ 60) mass infall rate than what is provided by competitive-like process.

The present molecular data were also used to study the amount of CO depletion and deuterium fractionation in the condensations. The CO depletion factors we derive, $f_D = 0.8 \pm 0.4 - 3.6 \pm 1.5$, do not suggest any significant CO freeze-out. However, these values are based on the canonical CO abundance of 9.5×10^{-5} relative to H_2 , whereas in Orion B this value can be considerably higher (by a factor of ~ 3). Therefore, at least an intermediate level of CO depletion seems possible in the condensations. The CO depletion timescale for the condensations ($\sim 2.2 \times 10^4$ yr) is shorter than the fragmentation timescale (by a factor of ~ 8) and the free-fall time of the condensations ($\sim 7 \times 10^4$ yr). Higher-resolution observations would undoubtedly reveal more CO-depleted condensation interiors. The derived N_2H^+ and N_2D^+ column densities lie in the range $0.7 - 2.5 \times 10^{13}$ and $2.5 - 7.6 \times 10^{12} \text{ cm}^{-2}$, and the corresponding fractional abundances are $\sim 0.9 - 2.3 \times 10^{-9}$ and $\sim 4.9 - 9.9 \times 10^{-10}$, respectively. The deuterium fractionation of N_2H^+ , or the $\text{N}_2\text{D}^+/\text{N}_2\text{H}^+$ column density ratio, lies in the range $0.30 \pm 0.07 - 0.43 \pm 0.09$. This is a stronger level of deuteration than is typically observed in starless/prestellar cores and should require significant gas-phase depletion of CO. The very high molecular deuteration observed towards the condensations suggests that they are in an advanced stage of chemical evolution and possibly on the verge of gravitational collapse. The actual fate of the subfragments, i.e., whether they can collapse into protostellar or substellar objects, remains to be elucidated. The lowest-mass condensations within SMM 6 could be the precursor sites of brown dwarf formation.

Acknowledgements. We are grateful to the staff at the APEX telescope for performing the service-mode heterodyne observations presented in this paper. We also appreciate the positive comments and insight of the anonymous referee. O. M. acknowledges the Academy of Finland for the financial support through grant 132291. S. S. R. O. acknowledges support from NASA through Hubble Fellowship grant HF-51311. This research has made use of NASA’s Astrophysics Data System and the NASA/IPAC Infrared Science Archive, which is operated by the JPL, California Institute of Technology, under contract with the NASA. SPIRE has been developed by a consortium of institutes led by Cardiff Univ. (UK) and including: Univ. Lethbridge (Canada); NAOC (China); CEA, LAM (France); IFSI, Univ. Padua (Italy); IAC (Spain); Stockholm Observatory (Sweden); Imperial College London, RAL, UCLMSSL, UKATC, Univ. Sussex (UK); and Caltech, JPL, NHSC, Univ. Colorado (USA). This development has been supported by national funding agencies: CSA (Canada); NAOC (China); CEA, CNES, CNRS (France); ASI (Italy); MCINN (Spain); SNSB (Sweden); STFC, UKSA (UK); and NASA (USA).

References

- André, P., Belloche, A., Motte, F., & Peretto, N. 2007, *A&A*, 472, 519 (ABMP07)
- André, P., Basu, S., & Inutsuka, S. 2009, in *Structure Formation in Astrophysics*, ed. Chabrier, G., Cambridge Univ. Press, p. 254
- André, P., Men’schikov, A., Bontemps, S., et al. 2010, *A&A*, 518, L102
- André, P., Ward-Thompson, D., & Greaves, J. 2012, *Science*, 337, 69
- Arzoumanian, D., André, P., Didelon, P., et al. 2011, *A&A*, 529, L6
- Bastien, P., Arcoragi, J.-P., Benz, W., et al. 1991, *ApJ*, 378, 255
- Belitsky, V., Lapkin, I., Vassilev, V., et al. 2007, in *Proceedings of joint 32nd International Conference on Infrared Millimeter Waves and 15th International Conference on Terahertz Electronics*, September 3-7, 2007, City Hall, Cardiff, Wales, UK, pp. 326-328
- Bergin, E. A., & Tafalla, M. 2007, *ARA&A*, 45, 339
- Bertoldi, F., & McKee, C. F. 1992, *ApJ*, 395, 140
- Bonnell, I. A., Bate, M. R., Clarke, C. J., & Pringle, J. E. 2001, *MNRAS*, 323, 785
- Bonnell, I. A., & Bate, M. R. 2006, *MNRAS*, 370, 488

- Caselli, P., Walmsley, C. M., Tafalla, M., et al. 1999, *ApJ*, 523, L165
- Caselli, P., Benson, P. J., Myers, P. C., & Tafalla, M. 2002, *ApJ*, 572, 238
- Chen, X., & Arce, H. G. 2010, *ApJ*, 720, L169
- Christie, H., Viti, S., Yates, J., et al. 2012, *MNRAS*, 422, 968
- Crapsi, A., Caselli, P., Walmsley, C. M., et al. 2004, *A&A*, 420, 957
- Crapsi, A., Caselli, P., Walmsley, C. M., et al. 2005, *ApJ*, 619, 379
- Dalgarno, A., & Lepp, S. 1984, *ApJ*, 287, L47
- Draine, B. T. 2011, *Physics of the Interstellar and Intergalactic Medium*, Princeton University Press
- Dubernet, M. L., Alexander, M. H., Ba, Y. A., et al. 2013, *A&A*, 553, A50
- Duchêne, G., & Kraus, A. L. 2013, *ARA&A*, *submitted*, arXiv:1303.3028
- Emprechtinger, M., Caselli, P., Volgenau, N. H., et al. 2009, *A&A*, 493, 89
- Fisher, R. T. 2004, *ApJ*, 600, 769
- Fontani, F., Caselli, P., Crapsi, A., et al. 2006, *A&A*, 460, 709
- Fontani, F., Giannetti, A., Beltrán, M. T., et al. 2012, *MNRAS*, 423, 2342
- Freking, M. A., Langer, W. D., & Wilson, R. W. 1982, *ApJ*, 262, 590
- Friesen, R. K., Kirk, H. M., & Shirley, Y. L. 2013, *ApJ*, 765, 59
- Fuller, G. A., & Ladd, E. F. 2002, *ApJ*, 573, 699
- Goodwin, S. P., Kroupa, P., Goodman, A., & Burkert, A. 2007, in *Protostars and Planets V*, eds. Reipurth, B., Jewitt, D., and Keil, K. (Tucson: Univ. of Arizona Press), p. 133
- Goodwin, S. P., Nutter, D., Kroupa, P., et al. 2008, *A&A*, 477, 823
- Güsten, R., Nyman, L. Å., Schilke, P., et al. 2006, *A&A*, 454, L13
- Hacar, A., & Tafalla, M. 2011, *A&A*, 533, A34
- Hartmann, L. 2002, *ApJ*, 578, 914
- Hill, T., Motte, F., Didelon, P., et al. 2011, *A&A*, 533, A94
- Hirota, T., Maezawa, H., & Yamamoto, S. 2004, *ApJ*, 617, 399
- Inutsuka, S.-I., & Miyama, S. M. 1992, *ApJ*, 388, 392
- Kamazaki, T., Saito, M., Hirano, N., & Kawabe, R. 2001, *ApJ*, 548, 278
- Kauffmann, J., Bertoldi, F., Bourke, T. L., et al. 2008, *A&A*, 487, 993
- Kauffmann, J., Bertoldi, F., Bourke, T. L., et al. 2011, *MNRAS*, 416, 2341
- Kirk, H., Johnstone, D., & Tafalla, M. 2007, *ApJ*, 668, 1042
- Kirk, J. M., Crutcher, R. M., & Ward-Thompson, D. 2009, *ApJ*, 701, 1044
- Kirk, H., Pineda, J. E., Johnstone, D., & Goodman, A. 2010, *ApJ*, 723, 457
- Kirk, H., Myers, P. C., Bourke, T. L., et al. 2013, *ApJ*, 766, 115
- Klein, B., Hochgürtel, S., Krämer, I., et al. 2012, *A&A*, 542, L3
- Kraus, A. L., & Hillenbrand, L. A. 2012, *ApJ*, 757, 141
- Kuiper, T. B. H., Langer, W. D., & Velusamy, T. 1996, *ApJ*, 468, 761
- Lacy, J. H., Knacke, R., Geballe, T. R., & Tokunaga, A. T. 1994, *ApJ*, 428, L69
- Ladd, E. F., Fuller, G. A., & Deane, J. R. 1998, *ApJ*, 495, 871
- Langer, W. D., Velusamy, T., Kuiper, T. B. H., et al. 1995, *ApJ*, 453, 293
- Larson, R. B. 1985, *MNRAS*, 214, 379
- Léger, A. 1983, *A&A*, 123, 271
- Lemme, C., Walmsley, C. M., Wilson, T. L., & Muders, D. 1995, *A&A*, 302, 509
- Luhman, K. L., Mamajek, E. E., Allen, P. R., et al. 2009, *ApJ*, 691, 1265
- Matzner, C. D., & McKee, C. F. 2000, *ApJ*, 545, 364
- Miettinen, O. 2012a, *A&A*, 540, A104
- Miettinen, O. 2012b, *A&A*, 545, A3
- Miettinen, O., & Offner, S. S. R. 2013, *A&A*, *in press*, arXiv:1304.0565
- Miettinen, O., Harju, J., Haikala, L. K., Kainulainen, J., & Johansson, L. E. B. 2009, *A&A*, 500, 845 (Paper I)
- Miettinen, O., Harju, J., Haikala, L. K., & Juvela, M. 2010, *A&A*, 524, A91 (Paper II)
- Miettinen, O., Harju, J., Haikala, L. K., & Juvela, M. 2012, *A&A*, 538, A137 (Paper III)
- Mollière, P., & Mordasini, C. 2012, *A&A*, 547, A105
- Nakamura, F., Takakuwa, S., & Kawabe, R. 2012, *ApJ*, 758, L25
- Offner, S. S. R., Krumholz, M. R., Klein, R. I., & McKee, C. F. 2008, *AJ*, 136, 404
- Offner, S. S. R., Hansen, C. E., & Krumholz, M. R. 2009, *ApJ*, 704, L124
- Offner, S. S. R., Kratter, K. M., Matzner, C. D., Krumholz, M. R., & Klein, R. I. 2010, *ApJ*, 725, 1485
- Ossenkopf, V., & Henning, T. 1994, *A&A*, 291, 943 (OH94)
- Ostriker, J. 1964, *ApJ*, 140, 1056
- Pagani, L., Bacmann, A., Cabrit, S., & Vastel, C. 2007, *A&A*, 467, 179
- Pagani, L., Daniel, F., & Dubernet, M.-L. 2009, *A&A*, 494, 719
- Palmeirim, P., André, P., Kirk, J., et al. 2013, *A&A*, 550, A38
- Peng, R., Langer, W. D., Velusamy, T., et al. 1998, *ApJ*, 497, 842
- Raghavan, D., McAlister, H. A., Henry, T. J., et al. 2010, *ApJS*, 190, 1
- Rawlings, J. M. C., Hartquist, T. W., Menten, K. M., & Williams, D. A. 1992, *MNRAS*, 255, 471
- Savva, D., Little, L. T., Phillips, R. R., & Gibb, A. G. 2003, *MNRAS*, 343, 259
- Schöier, F. L., van der Tak, F. F. S., van Dishoeck, E. F., & Black, J. H. 2005, *A&A*, 432, 369
- Schnee, S., Enoch, M., Johnstone, D., et al. 2010, *ApJ*, 718, 306
- Shu, F. H. 1977, *ApJ*, 214, 488
- Stamatellos, D., & Whitworth, A. P. 2003, *A&A*, 407, 941
- Stamatellos, D., & Whitworth, A. P. 2009, *MNRAS*, 392, 413
- Tafalla, M., & Santiago, J. 2004, *A&A*, 414, L53
- Tafalla, M., Myers, P. C., Caselli, P., & Walmsley, C. M. 2004, *A&A*, 416, 191
- Takakuwa, S., Mikami, H., & Saito, M. 1998, *ApJ*, 501, 723
- Takakuwa, S., Kamazaki, T., Saito, M., & Hirano, N. 2003, *ApJ*, 584, 818
- Tohline, J. E. 2002, *ARA&A*, 40, 349
- van der Tak, F. F. S., Black, J. H., Schöier, F. L., et al. 2007, *A&A*, 468, 627
- Vassilev, V., Meledin, D., Lapkin, I., et al. 2008a, *A&A*, 490, 1157
- Vassilev, V., Henke, D., Lapkin, I., et al. 2008b, *IEEE Microwave and Wireless Components Letters*, pp. 55-60, Vol. 18, Number 1
- Ward-Thompson, D., Scott, P. F., Hills, R. E., & André, P. 1994, *MNRAS*, 268, 276
- Whitworth, A. P., & Stamatellos, D. 2006, *A&A*, 458, 817
- Williams, J. P., de Geus, E. J., & Blitz, L. 1994, *ApJ*, 428, 693
- Wiseman, J. J., & Ho, P. T. P. 1998, *ApJ*, 502, 676

Appendix A: Revision of core/condensation properties presented in Paper III

In Paper III, the condensation masses and densities were estimated assuming that T_{dust} equaled the T_{kin} derived towards the selected position near the edge of SMM 6, i.e., 11.0 ± 0.4 K. However, all the subcondensations except SMM 6a lie outside the $40''$ beam of the NH_3 measurements used to derive T_{kin} . Moreover, T_{dust} is expected to be lower in the embedded small condensations because they are better shielded from the external dust heating radiation field. On these grounds, we revise the temperature-dependent condensation properties by assuming that $T_{\text{dust}} = 10$ K. This seems a reasonable choice given that the gas temperature is about 11 K at the core edge.

In addition, it was previously assumed that the $350\text{-}\mu\text{m}$ dust mass absorption (or emission) coefficient, i.e., the dust opacity per unit dust mass, was $\kappa_{350\mu\text{m}} = 10 \text{ cm}^2 \text{ g}^{-1}$. This value was interpolated from the widely used Ossenkopf & Henning (1994, hereafter OH94) model describing graphite-silicate dust grains that have coagulated and accreted *thick* ice mantles over a period of 10^5 yr at a gas density of $n_{\text{H}} = 10^5 \text{ cm}^{-3}$. If we assume that grains have *thin* ice mantles, which might be more appropriate here (e.g., Stamatellos & Whitworth 2003 and references therein)⁸, $\kappa_{350\mu\text{m}}$ is decreased to $7.84 \text{ cm}^2 \text{ g}^{-1}$. In Paper III, the dust-to-gas ratio was assumed to be 1/100. However, this value refers to the canonical dust-to-hydrogen mass ratio, $M_{\text{dust}}/M_{\text{H}}$ (e.g., Draine 2011; Table 23.1 therein). If we assume solar composition, i.e., the mass fractions for hydrogen, helium, and heavier elements are $X = 0.71$, $Y = 0.27$, and $Z = 0.02$, respectively, the ratio of total mass (H+He+metals) to hydrogen mass is $1/X \approx 1.41$. The total dust-to-gas mass ratio is therefore $M_{\text{dust}}/M_{\text{gas}} = M_{\text{dust}}/(1.41M_{\text{H}}) = 1/141$. We note that for the assumed gas composition, the mean molecular weight per free particle is $\mu_{\text{p}} = 2.37$ and that per H_2 molecule is $\mu_{\text{H}_2} \approx 2.82$ (Kauffmann et al. 2008; Appendix A.1 therein).

The masses (M), peak beam-averaged H_2 column densities [$N(\text{H}_2)$], and averaged H_2 number densities [$\langle n(\text{H}_2) \rangle$] were computed using the standard optically thin dust emission formulation [see, e.g., Eqs. (2) and (3) in Paper I, and Eq. (1) in Paper III]. The results are given in Table 1. The uncertainties in M and $N(\text{H}_2)$ were propagated from the uncertainties in the integrated flux density and the peak surface brightness, respectively. We note that the uncertainty in dust opacity, which is likely a factor $\gtrsim 2$, is the major source of error in the mass and column density estimate. The error in $\langle n(\text{H}_2) \rangle$ was propagated from that of M .

We note that the total mass of the SMM 6 core was previously determined from the LABOCA $870\text{-}\mu\text{m}$ emission adopting the thick ice mantle model of OH94, in which case $\kappa_{870\mu\text{m}} \approx 1.7$

⁸ The assumption of thin ice mantles is supported by the fact that no significant CO depletion is found in the present study (see Sect. 4.6).

$\text{cm}^2 \text{g}^{-1}$. If we employ the above thin ice mantle model, $\kappa_{870\mu\text{m}}$ is $1.38 \text{ cm}^2 \text{g}^{-1}$. Moreover, the $870\text{-}\mu\text{m}$ flux density of the source, when integrated inside the $0.09 \text{ Jy beam}^{-1}$ or 3σ contour of the re-reduced LABOCA map (see Miettinen & Offner 2013), is $S_{870\mu\text{m}} = 1.03 \pm 0.22 \text{ Jy}$. For $T_{\text{dust}} = 11.0 \pm 0.4 \text{ K}$ and $M_{\text{dust}}/M_{\text{gas}} = 1/141$, these revisions yield a mass of $5.9 \pm 1.3 M_{\odot}$, a factor of 1.4 lower than reported previously (see Paper II). The discrepancy mostly stems from the larger area previously used to compute $S_{870\mu\text{m}}$. The virial parameter of the core from Paper II is accordingly revised to $\alpha_{\text{vir}} = 1.1 \pm 0.2$, which still satisfies the gravitational boundedness condition of $\alpha_{\text{vir}} < 2$ and is very close to virial equilibrium ($\alpha_{\text{vir}} = 1$). Therefore, the source can be considered a candidate prestellar core (cf. Sect. 4.2).

The projected length of the SMM 6 filament along its long axis, as measured from the *Herschel* $250\text{-}\mu\text{m}$ emission shown in Fig. 1, is about $1'.7$ or $L = 0.22 \text{ pc}$. This corresponds to the extent of the 3σ LABOCA $870\text{-}\mu\text{m}$ emission (Paper III; Fig. 9 therein). The corresponding mass per unit length, or line mass, is $M_{\text{line}} \approx 27 \pm 6 M_{\odot} \text{ pc}^{-1}$.